



Effect of Mo content on the corrosion resistance of $(\text{CoCrFeNi})_{1-x}\text{Mo}_x$ thin films in sulfuric acid

Clara Linder^{a,b,*}, Smita G. Rao^c, Robert Boyd^b, Grzegorz Greczynski^c, Per Eklund^c, Sara Munktel^d, Arnaud le Febvrier^c, Emma M. Björk^b

^a RISE, Corrosion, Vehicles and Surface Protection, 164 40, Kista, Sweden

^b Nanostructured Materials, Department of Physics, Chemistry and Biology (IFM), Linköping University, 581 83, Linköping, Sweden

^c Thin Film Physics Division, Department of Physics, Chemistry, and Biology (IFM), Linköping University, 581 83, Linköping, Sweden

^d Swerim AB, Metallic materials in corrosive environments, 164 40, Kista, Sweden

ARTICLE INFO

Key words:

Magnetron sputtering
Multicomponent thin film
High entropy alloy
Corrosion, Fuel cells

ABSTRACT

$(\text{CoCrFeNi})_{1-x}\text{Mo}_x$ thin films with various Mo content (0–10 at.%) were grown by magnetron sputtering on a stainless steel substrate. The films with 0–2 at.% presented two crystal structures: one FCC phase and one sigma phase, while films with higher Mo content only had the FCC structure. All films have a (111) texture and follow the topography of the substrate. The corrosion resistance of the films was evaluated in 0.05 M H_2SO_4 at room temperature and at 80 °C. It was observed that the corrosion current densities considerably decreased for Mo > 2 at%, and that the current densities were higher at the elevated temperature. Scanning Kelvin Probe Force Microscopy showed a large potential difference between the main FCC phase and sigma phase for the Mo0–2 films. This would suggest that preferential dissolution of the FCC phase occurs over the sigma and reduces the corrosion resistance. Such preferential dissolution does not occur for the higher Mo content films with only the FCC phase. The high corrosion resistance was also attributed to the inhibition of Fe and Cr dissolution by Mo and the stabilisation of the Cr enriched oxide by incorporating Mo oxides into the passive film, identified by X-ray photoelectron spectroscopy. The low corrosion current densities (below 1 $\mu\text{A}/\text{cm}^2$) make these thin films possible candidates for protective coatings of bipolar plates in PEM fuel cells.

1. Introduction

Proton Exchange Membrane (PEM) fuel cells require materials that can withstand the acidic and highly corrosive environment present inside the cell [1–3]. Bipolar plates separate the electrodes inside the fuel cell and lead the fuel to the active membranes, and are typically made from stamped stainless-steel sheets [4]. However, the corrosion resistance of these sheets is often insufficient and, therefore, there is a need to find protective coating materials [2].

Multicomponent materials, in particular High Entropy Alloy (HEA) thin films, have mechanical properties, such as hardness and corrosion resistance, superior to conventional materials such as steels and nickel alloys. Refractory HEA thin films, such as $(\text{CrNbTaTiW})\text{C}$ [5] and $\text{TiNbZrTa}_x\text{N}_x$ [6] have a high corrosion resistance in HCl and H_2SO_4 . These materials are designed for high temperature and high hardness applications [7]. PEM fuel cells, however, operate at room to medium temperatures (<100 °C) and the coated bipolar plates should have high

formability. Other HEA alloys are more suitable for these applications, such as the Cantor alloy CoCrFeNiMn [8] and its variants. It has been shown that the alloys CoCrNi and CoCrFeNi [9–11] have better corrosion resistance than stainless steels 316 L and 304 in H_2SO_4 . Variants of the Cantor alloy have been made as coatings, for example AlCrFeCoCuNiTi by laser cladding [12] showed higher corrosion resistance than stainless steel 304 and other HEAs in both H_2SO_4 and HCl. CoCrNi coatings produced by spark plasma sintering of powder [13] were also found to be highly corrosion resistant in H_2SO_4 .

Small additions of molybdenum (Mo) to stainless steel can considerably increase the corrosion resistance of the material. The Pitting Resistance Equivalent Number (PREN) is commonly used to compare different materials in terms of corrosion [14] and is calculated from the material composition. The Mo content is taken into account for PREN as Mo increases the pitting resistance of stainless steels [15]. For example, steel grade 316 only differentiates in composition from grade 304 by adding 2 wt% Mo [14], and 316 has a higher pitting resistance in

* Corresponding author.

E-mail addresses: clara.linder@ri.se, clara.linder@liu.se (C. Linder).

<https://doi.org/10.1016/j.tsf.2024.140220>

Received 12 September 2023; Received in revised form 1 November 2023; Accepted 13 January 2024

Available online 14 January 2024

0040-6090/© 2024 The Authors. Published by Elsevier B.V. This is an open access article under the CC BY license (<http://creativecommons.org/licenses/by/4.0/>).

chloride containing environments [16]. This is also valid for HEA alloys and the Cantor variant. CrFeMoNiRuW alloys showed similar corrosion behaviour to superalloy C-22 in H_2SO_4 and high pitting resistance in HCl. This was attributed to the formation of stable oxides with low dissolution rate into the electrolyte [17]. The beneficial effect of Mo has also been seen for uniform corrosion mechanisms in acidic media. For example, adding Mo to CoCrFeNi considerably increased the corrosion resistance of the alloy in H_2SO_4 , and made it more resistant than stainless steel 316 L [18]. Furthermore, increasing the Mo content in a CoCrFeMo_xNi alloy decreased the corrosion current density, i.e. the corrosion rate in H_2SO_4 [19,20]. Similar effects of Mo addition have been observed for CoCrFeMoNi coatings. For example, the corrosion resistance in NaCl of CoCrFeMoNi deposited by magnetron sputtering [21], thermal spraying [22] and laser cladding [23] was significantly improved by Mo addition and superior to 304 and 316 stainless steels. However, the corrosion resistance in acidic environment of (CoCrFeNi)_{1-x}Mo_x thin films deposited by magnetron sputtering and the effect of a Mo composition gradient has not yet been fully reported.

In this work, we study (CoCrFeNi)_{1-x}Mo_x thin films, as thin coatings (<1 µm) are required for bipolar plates in fuel cells. The effect of Mo concentration on the film structure, and how it correlates to the corrosion properties has been investigated. The corrosion properties of the films were investigated in sulfuric acid to get an indication if the Mo introduction enables utilization of the films in a PEM fuel cell.

2. Materials and methods

2.1. Thin film synthesis

Cold rolled and bright annealed 304 L stainless steel sheets (30 × 30 × 1 mm) with an average roughness of 85 nm were used as received as substrates. Before the depositions the substrates were ultrasonically cleaned in acetone then isopropanol. (CoCrFeNi)_{1-x}Mo_x thin films were deposited by direct current magnetron sputtering. The deposition system is equipped with four 30° inclined magnetrons (details about the sputtering apparatus can be found elsewhere [24]) and the base pressure in the chamber was <10⁻⁷ Pa. Two 50-mm-diameter targets were used: one CoCrFeNi compound target (Plansee, Composite Materials GmbH) and one elemental Mo target. The power applied to the Mo target was varied from 0 to 12 W. The power applied to the compound target was adjusted accordingly so that the total power applied to the targets was kept constant at 100 W. Argon gas was introduced at each magnetron with a total flow of 90 sccm corresponding to a process pressure of 0.53 Pa. The substrate was rotated at 15 rpm during the deposition to ensure uniform deposition. A substrate bias of -100 V was applied. The depositions were carried out at room temperature for 20 min, resulting in a film thickness of approximately 130 nm for all films.

2.2. Structural and chemical characterisation

The crystal structure of the films was characterised by X-ray diffraction (XRD) using a Bruker D8 Discover diffractometer in a symmetric $\theta/2\theta$ configuration and Cu K α X-ray source ($\lambda = 1.5406$ Å). The morphology and chemical composition of the thin films were analysed using scanning electron microscopy (SEM) Sigma 70 and Sigma 300 VP Gemini (Zeiss, 5 kV acceleration voltage), and an energy dispersive spectroscopy (EDS) detector (Oxford Instruments X-MAX^N, 5 kV acceleration voltage) integrated in the microscope. Additional SEM analysis, including in lens back scattered imaging and electron backscattered diffraction, was performed on a Zeiss 560 Gemini instrument fitted with a Symmetry S2 (Oxford instruments) diffractometer.

Cross-sectional samples suitable for analysis both by SEM and (scanning) transmission Electron Microscopy ((S)TEM) were prepared using a dual beam SEM-Focused Ion Beam (FIB) microscope (Gemini Zeiss 1540 EsB). Pt layers were first deposited on top of the surface of the films to protect them during milling. SEM images of the cross sections

were taken using the same instrument using a 36° image correction to take account of the sample tilt. Thin lamella (<100 nm) suitable for TEM analysis were prepared using the well-established lift-out approach. TEM analysis was performed using a FEI Tecnai G2 TF 20 UT microscope operated at 200 kV acceleration voltage. Dark field STEM images were taken with an angular detector.

Scanning Kelvin Probe Force Microscopy (SKPFM) was used to measure potential maps of the samples in addition to the height maps obtained through atomic force microscopy (AFM). A Bruker Dimension Icon AFM microscope was used in frequency modulation mode (FM-KFM). A PtIr coated Si tip, with a 200–250 µm length and resonance frequency of 60–100 kHz, was used for the measurements. The results were analysed using the software NanoScope analysis V1.9.

X-ray photoelectron spectroscopy (XPS) was used for elemental analysis and assessment of chemical bonding. O 1 s, Co 2p, Cr 2p, Fe 2p, Mo 3d and Ni 2p core level spectra were recorded using an Axis Ultra DLD instrument from Kratos Analytical (UK) employing monochromatic Al K α radiation ($h\nu = 1486.6$ eV) and an anode power of 150 W. The base pressure during spectra acquisition was lower than 1.5×10^{-7} Pa (1.1×10^{-9} Torr). No charge compensation was used during analysis. The analyser pass energy was set to 20 eV resulting in the full width at half maximum of 0.55 eV for the Ag 3d_{5/2} peak of sputter-etched Ag sample used for calibration. All spectra were collected at normal emission angles. The area analysed by XPS was 0.3×0.7 mm². As the commonly used charge referencing method relying on the C 1 s peak of adventitious carbon is not reliable [25], all spectra were referenced to the sample Fermi edge. Spectra deconvolution and quantification is performed using CasaXPS software package (version 2.3.16) and sensitivity factors supplied by the instrument manufacturer. After linear background subtraction the core level spectra were fitted using Voigt functions. The model constraints include: (i) the full-width-at-half-maximum (FWHM) is the same for both peaks that belong to the same doublet, (ii) 2:1 intensity ratios are preserved between 2p_{3/2} and 2p_{1/2} spin-split components, (iii) the binding energy splitting between 2p_{3/2} and 2p_{1/2} peaks in the spectra from metals is fixed.

2.3. Electrochemical measurements

The films were immersed in an acidic environment (0.05 M H_2SO_4 adjusted pH to 3 ± 0.1) at room temperature and at 80 °C to investigate their corrosion properties. Electrochemical measurements were carried out with a PARSTAT 3000A-DX potentiostat. A three-electrode set-up was used where the working electrode was the thin film, an Ag/AgCl saturated with KCl ($E = 0.197$ V vs SHE) was used as reference electrode and a Pt wire as the counter electrode. The open circuit potential (OCP) was first measured for 30 min. Potentiodynamic polarisation (PD) was carried out from -0.25 V vs OCP to 1.6 V with a scan rate of 1 mV/s. The Tafel module in the software VersaStudio was used to calculate the Tafel

Table 1

Average composition of the films determined by EDS and the compound target.

Mo target power (W)	Sample name	Composition (At.%)				
		Cr	Fe	Co	Ni	Mo
0	Mo0	19.4 ± 0.3	29.8 ± 0.1	28.4 ± 0.8	22.3 ± 0.7	0
3	Mo2	21.3 ± 0.3	29.0 ± 0.2	26.8 ± 0.2	21.0 ± 0.3	1.9 ± 0.1
6	Mo4	19.5 ± 0.5	28.9 ± 0.2	26.5 ± 0.3	20.7 ± 0.2	4.4 ± 0.1
9	Mo7	20.3 ± 0.4	27.6 ± 0.0	25.7 ± 0.1	19.6 ± 0.2	6.8 ± 0.2
12	Mo10	18.3 ± 0.3	27.5 ± 0.1	25.3 ± 0.3	19.0 ± 0.3	9.9 ± 0.3
–	Compound target	24.0	32.0	24.0	20.0	–

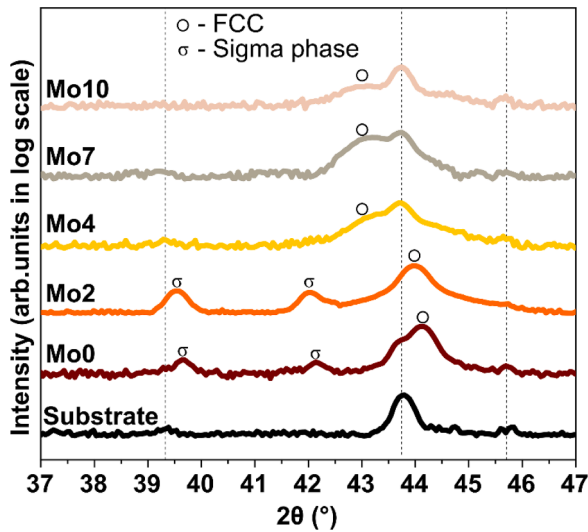


Fig. 1. X-ray diffractograms for all films and the substrate. Dotted lines indicate the peaks from the substrate. Symbols indicate the FCC and sigma phases in the films.

slopes and determine the corrosion current density I_{corr} . The extrapolation was carried out 0.1 V away from E_{corr} . All measurements were repeated for duplicate samples. To investigate the evolution of the passive film when exposed to the acidic electrolyte, the samples were polarised at 0.4 V for 1 h to passivate the films and then analysed with XPS.

3. Results

3.1. Thin film structure

The Mo content was varied in the films by applying different powers

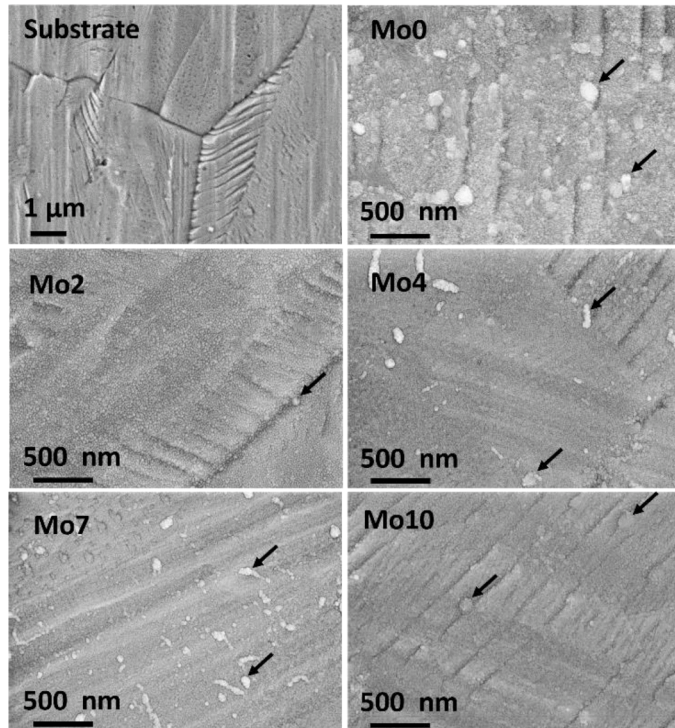


Fig. 2. SEM micrographs of the surface of the substrate and films with various Mo content. Arrows indicate examples of agglomerates.

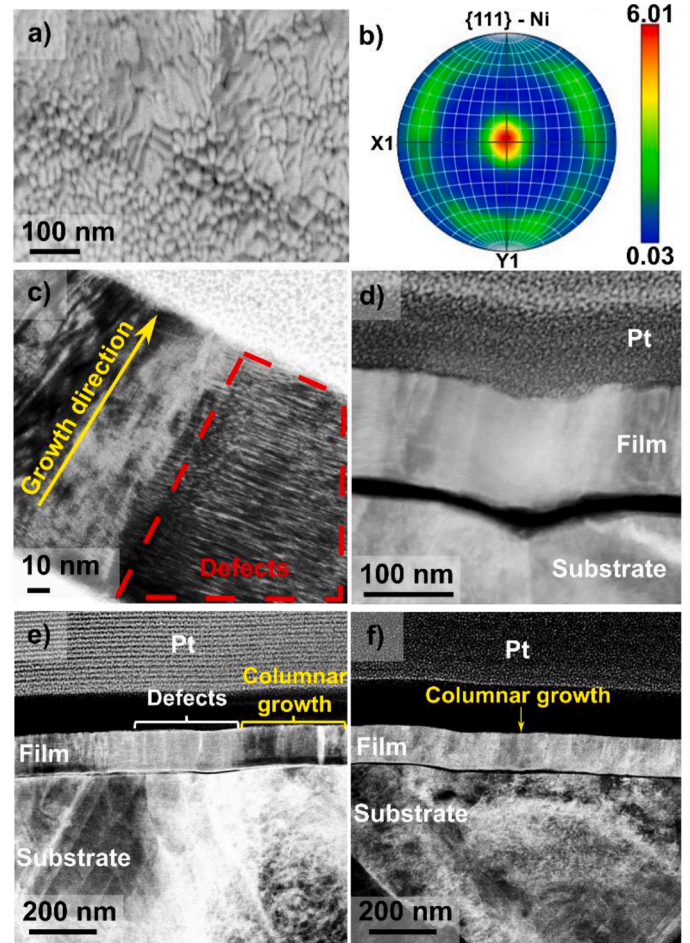


Fig. 3. a) High magnification back scattered SEM image of Mo0 film at substrate grain boundary, b) EBSD pole figure for the Mo0 film, c) TEM cross-section image of the Mo0 film, a columnar structure to the left and an elongated structure with defects circled with a dotted line d) Dark field STEM cross-section image of the Mo0 film e) STEM image of Mo2 film with both the columnar and defect structures f) STEM image of Mo4 with only the columnar structure.

to the Mo target (0, 3, 6, 9, 12 W). The composition of the films was determined using EDS. The names and average composition for each film is given in Table 1.

X-ray diffractograms of the films are shown in Fig. 1. The peak observed at $2\theta \approx 44^\circ$ corresponds to the 111 reflections of a FCC phase which is in agreement with previous studies [18,19,23]. As the Mo content is increased from 2 at.%, an angular shift of the peak from 44° to 43° for films with higher Mo content is observed. The shift is attributed to the lattice expansion when more Mo is introduced into the lattice. The lattice parameters calculated using Bragg's law are 3.84 Å for Mo content <2 at.% and 3.91 Å for higher Mo content. For Mo content <2 at.% a secondary sigma phase with reflections at 39° and 42° was also observed. This phase has been observed in CoCrFeNi thin films deposited at room temperature and CoCrFeNi alloys [26,27].

Fig. 2 shows SEM micrographs of the films' surface. There is no apparent difference in terms of film morphology when the Mo content is varied. The parallel lines along the apparent grain boundaries of the substrate are slip bands as a result of cold rolling [28,29]. Agglomerates with the same composition as the films were observed for all films. Films grown on Si wafers do not display these agglomerates (shown elsewhere [30]), and therefore it was concluded that the film growth was influenced by the structural defects or topography of the stainless-steel substrate itself.

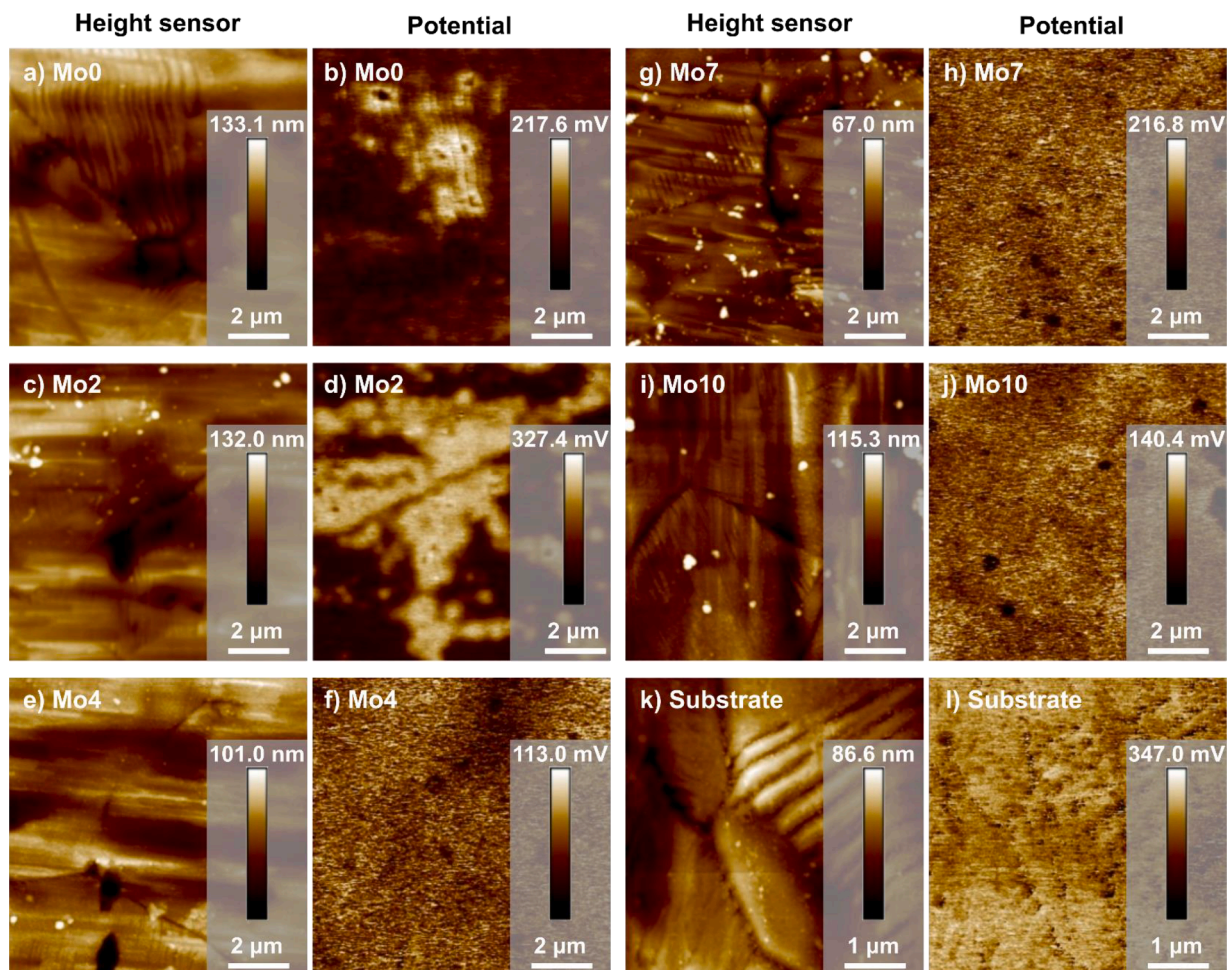


Fig. 4. Height maps (a, c, e, g, i and k) and potentials maps (b, d, f, h, j, l) for Mo0–10 and the bare substrate.

To further characterise the films and show the different structures within the films, higher magnification SEM micrographs and cross-sectional TEM and STEM images were acquired, shown in Fig. 3.

Fig. 3a shows the planar SEM image of the Mo0 film close to a substrate grain boundary. The grains are seen to be orientated different directions depending on the substrate morphology. Fig. 3b shows the EBSD pole figure of Mo0 film. The pattern was indexed to a Ni FCC crystal with a (111) texture. Fig. 3c shows a TEM micrograph of Mo0 where two grain structures are visible. One is a columnar structure, typical for PVD deposited thin films. The other (circled by the dotted line) is a more elongated structure with the same crystal structure and orientation, which is a region with high amounts of defects such as stacking faults. In the STEM dark field image in Fig. 3d a detachment of the film is visible from the substrate grain boundary, indicating poor adhesion of the film to the substrate. The two structures, i.e. columnar and elongated are also visible. The elongated are located at the centre of the image, right above the substrate grain boundary. Similar structures were also observed for Mo2 (Fig. 3e). For Mo4–10 only the columnar grains were present (micrographs of Mo4 available in Fig. 3f). The film thickness was measured to be approximately 130 nm. Overall, the grains in the films are orientated along the substrate morphology but have a (111) texture and there are two types of structures (columnar and elongated grains) within the Mo0 and Mo2 films.

Fig. 4 shows the height and potential maps obtained by SKPFM on as-deposited films Mo0, Mo2 and Mo10.

Significant potential differences are visible on the micrometre level

and seem closely linked to the substrate morphology. For Mo0, the areas closest to the grain boundaries of the substrate, in particular where the slip bands are visible, have a higher potential compared to the rest of the film. Areas with different potential values becomes larger and more evident when Mo is added (Fig. 4d). However, when the Mo content is further increased (>2 at%) this effect is no longer visible (Fig. 4f, h, and j). This potential gradient is not observed for the bare substrate (Fig. 4l). Differences in Volta potentials are often related to different crystal structures [31].

3.2. Corrosion resistance at room temperature

Fig. 5 shows typical polarisation curves recorded for the different films in H₂SO₄ pH 3 at room temperature. All tested films have a passive region and a transpassive region. The corrosion potentials for the films are close to each other and around 0 to −0.1 V vs Ag/AgCl. The passive region starts directly after the corrosion potential as no active-passive peak is observed, i.e. the passive film is stable after E_{corr} . The passive region extends until 0.85 V for all films. Above this potential, the transpassive region is reached with an abrupt increase of the current density indicating the break-down of the passive film. This region also corresponds to the onset of the oxygen evolution reaction which contributes to the current density. A peak at 1.3 V is visible for all films and is corresponding to the start of the repassivation of the films, as the current density decreases after this potential [32]. However, the reformed passive film is not stable at higher potentials (>1.5 V) as the

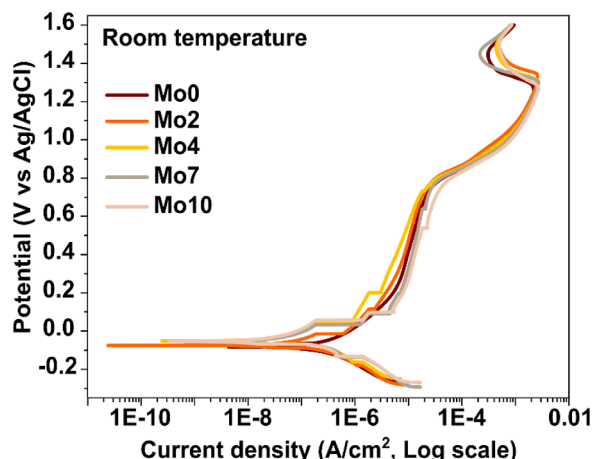


Fig. 5. Potentiodynamic polarisation curves recorded for the films in 0.05 M H_2SO_4 pH 3 at room temperature, scan rate 1 mV/s. Plateaus around the E_{corr} ($-0.2 - 0.2$ V) are related to noise in the signal.

current density increases again, indicating film dissolution.

The E_{corr} and corrosion current density I_{corr} values were extracted through Tafel extrapolation and are presented in Table 2.

The corrosion potential E_{corr} is in the same range for the films. The corrosion current densities are ~ 220 nA/cm² for all films at room temperature. The passive current density is ~ 7 $\mu\text{A}/\text{cm}^2$ for Mo0–4 and slightly higher for Mo7 and Mo10 (9 and 13 $\mu\text{A}/\text{cm}^2$ respectively). The breakdown potential is around 850 mV for all films, except Mo10 for which it is lower at 830 mV. This would indicate that Mo10 has a slightly lower corrosion resistance, given that the passive current density is higher than the other samples and the breakdown potential is lower. This could be due to the higher Mo/Cr ratio, i.e. less Cr available in the passive film which would reduce the protective ability of the passive film for Mo10.

Analysis of the films after the polarisation at room temperature reveal the films containing Mo had partially peeled off, whereas the film without Mo had completely peeled off (observable by naked eye after

electrochemical measurements). The peeling-off was observed after polarisation in the transpassive region which would indicate that the passive film has broken down and the dissolution can occur freely. SEM micrographs for Mo10 are shown in Fig. 6. EDS analysis of the remaining films indicates that the corrosion products (darker regions in SEM image) contain mainly Mo, Fe, Cr, Ni and O whereas Co is only present in form of small agglomerates (light particles in SEM image).

Fig. 7 shows XPS spectra acquired from the as deposited (pristine) films and passivated films at 0.4 V in H_2SO_4 at room temperature. The passivation potential was selected in the passive region of the polarisation curves shown in Fig. 5. Quantification was carried out to determine the at% of the oxide films and is shown in Table 3.

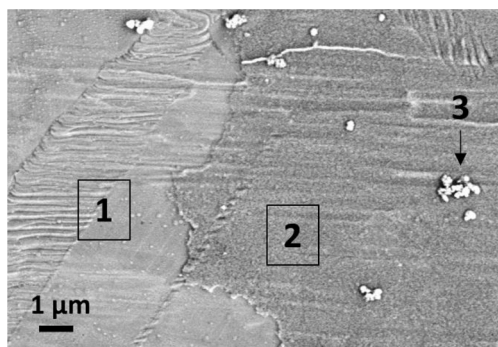
The native oxide formed on the as-deposited films appears to be a mix of Mo, Cr, Fe, Co and Ni oxidised species. The oxide peaks in Fe 2p and Cr 2p spectra increase with increasing Mo content. Different behaviours are observed in the Co 2p signal: the oxide peaks increase for the Mo0–2 films and decrease again for the Mo4–10 films, which could also be seen in the quantification. Ni 2p shows relatively small peak intensities for oxidised species, much weaker compared to the other elements. For Mo 3d, the total signal increases with increased Mo content showing both metal and oxide peaks. Mo 3d can be deconvoluted into two peaks for Mo(IV) (long dash) and Mo(VI) (short dash) oxide species. All O 1s spectra exhibit two distinct peaks. The lower binding energy component is assigned to the metal-oxide, while the high binding component is assigned to metal-hydroxide. There is also contribution from C–O, C = O species at 530 eV due to surface contamination layers.

After passivation, the relative intensity of Cr 2p peaks increased considerably and the Cr at% in the oxide increased. The hydroxide peak become more intense than the oxide peak as compared to the spectra recorded from pristine films. Furthermore, for all films the O 1s spectra show more intense hydroxide peaks compared to the native film and the oxygen content in the oxide increased as well. For Mo0 and Mo4 the hydroxide peak is higher than its oxide peak. Co 2p and Fe 2p spectra reveal that the intensity of the oxide peaks in all films is lower after passivation and the Fe and Co at% in the oxide film decreased. Similar trend is observed in Ni 2p spectra from Mo0–4 films. However, Ni 2p spectra from films with the highest Mo content (Mo7–10) show new peaks at binding energy of 874 eV, which may indicate higher oxidation

Table 2

Corrosion potential (E_{corr}) corrosion current density (I_{corr}), passive current density (I_{pass}) and transpassive breakdown potential (E_{trans}) extracted from polarisation curves in Fig. 5.

	Mo0	Mo2	Mo4	Mo7	Mo10
E_{corr} (mV) RT	-76 ± 6	-59 ± 20	-44 ± 9	-53 ± 2	-48 ± 19
I_{corr} (nA/cm ²) RT	262 ± 53	230 ± 43	196 ± 58	203 ± 11	216 ± 30
I_{pass} ($\mu\text{A}/\text{cm}^2$) RT	7.9 ± 1.7	6.8 ± 1.1	7.0 ± 0.9	9.4 ± 1.8	13 ± 0.1
E_{trans} (mV) RT	847 ± 2	859 ± 7	850 ± 6	847 ± 4	831 ± 2



At%	O	Cr	Fe	Co	Ni	Mo
1	1.1	20.9	67.9	0.0	9.6	0.0
2	11.7	22.2	54.9	0.1	7.6	3.5
3	12.0	17.6	29.3	19.1	16.0	5.9

Fig. 6. SEM micrographs of the surface of the Mo10 film after polarisation up to 1.6 V vs Ag/AgCl. Area 1 is the substrate, 2 the remaining film and 3 the macroparticles.

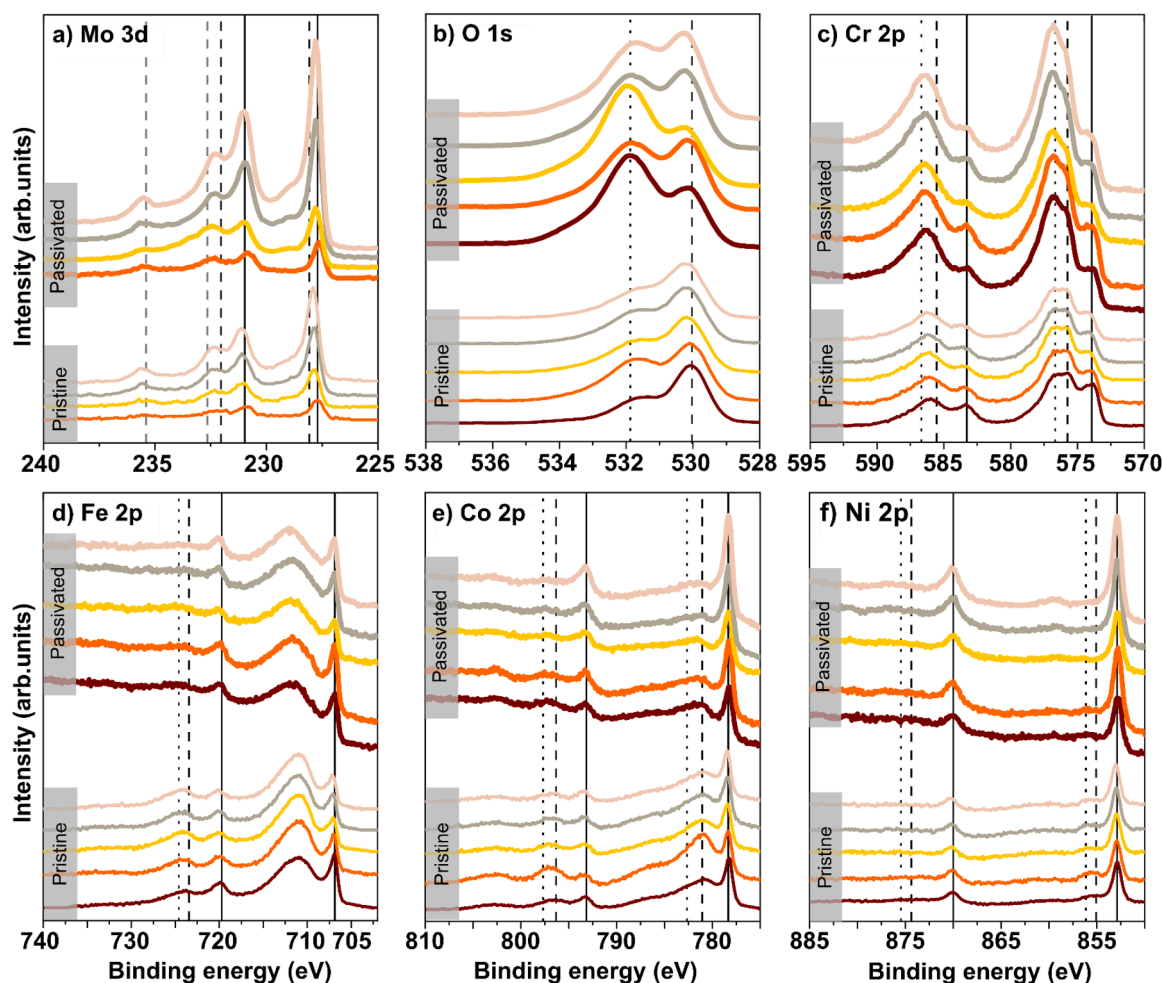


Fig. 7. High resolution core-level spectra a) Mo 3d, b) O 1s c) Cr 2p, d) Fe 2p, e) Co 2p, and f) Ni 2p of as-deposited films (pristine) and after passivation at 0.4 V in H_2SO_4 . Solid lines indicate the metallic components, dashed lines the oxide species and dotted lines the hydroxide species.

Table 3
XPS quantification of native oxide and passivated film extracted from Fig. 7.

At%	Sample name	Co	Cr	Fe	Mo	Ni	O
Native oxide	Mo0	16.8	14.5	5.9	0	5.9	37.9
	Mo2	14.7	11.2	19.7	0.8	4.1	49.4
	Mo4	11.7	12	23	1.9	4.8	46.7
	Mo7	13.7	12.2	20.2	3.4	3.9	46.6
	Mo10	13	11.6	20.7	4.5	4.5	45.8
Passivated	Mo0	9.7	14.3	11.5	0	4.6	59.9
	Mo2	8.3	17.3	16.6	1.2	5.8	50.8
	Mo4	5.3	13.2	11.7	2.5	5.3	62
	Mo7	6.8	16.7	13.6	4.4	4.2	54.2
	Mo10	6.8	17.6	12.6	5.7	5.1	52.2

states such as Ni_2O_3 [33]. For Mo 3d spectrum, the peak intensities remain the same after passivation and so does the Mo content. Above changes indicate that the native oxide continues to grow under polarisation. After passivation, it is composed of mainly Cr and Mo oxide, Cr hydroxide species and to lesser extents Fe, Co and Ni oxides.

3.3. Corrosion resistance at 80 °C

The operating temperature of a PEM fuel cells is usually around 80 °C. To ensure the films' corrosion resistance is sufficient at higher temperature, potentiodynamic polarisation was carried out at 80 °C and are shown in Fig. 8.

The shape of the polarisation curve is very similar to the ones at room temperature, indicating the films have the same corrosion behaviour regardless of temperature. Differences between the films becomes clearer at 80 °C, i.e. the difference in corrosion potential and current density are more significant as it can be seen in Table 4. There are more differences in current densities in the passive region of the films (0.2 V–0.85 V) at 80 °C compared to room temperature. The current density decreases with added Mo, which can also be seen in Table 4.

The corrosion potential and breakdown potentials at 80 °C are slightly lower compared to the room temperature condition. For Mo contents >4.4 at% the current densities are significantly decreased compared to films with lower Mo contents. The passive current density decreases with added Mo, from 30 to 15 $\mu\text{A}/\text{cm}^2$ by adding 2 at% Mo and even further for Mo > 4 at.% approximately 10 $\mu\text{A}/\text{cm}^2$. The breakdown potential does not follow this trend.

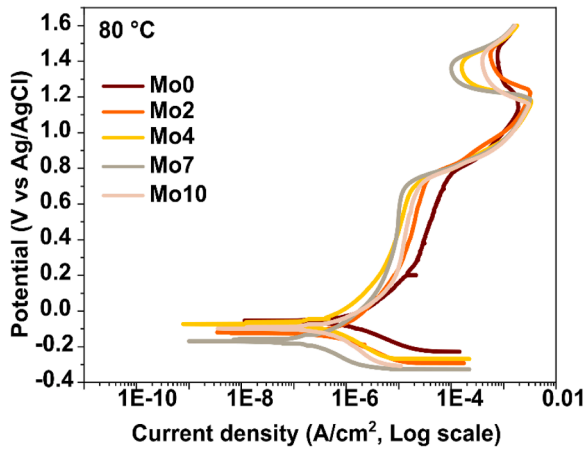


Fig. 8. Potentiodynamic polarisation curves recorded for the films in 0.05 M H_2SO_4 pH 3 at 80 °C, scan rate 1 mV/s.

Table 4

Corrosion potential (E_{corr}), corrosion current density (I_{corr}), passive current density (I_{pass}) and transpassive breakdown potential (E_{trans}) extracted from polarisation curves in Fig. 8.

	Mo0	Mo2	Mo4	Mo7	Mo10
E_{corr} (mV) 80 °C	-82 ± 9	-101 ± 23	-75 ± 23	-143 ± 37	-70 ± 38
I_{corr} (nA/cm ²) 80 °C	1226 ± 31	635 ± 30	451 ± 14	354 ± 78	405 ± 62
I_{pass} (μA/cm ²) 80 °C	31.6 ± 0.3	15.8 ± 0.7	10.3 ± 1.7	8.6 ± 0.2	10.6 ± 2.1
E_{trans} (mV) 80 °C	792 ± 6	805 ± 7	796 ± 2	800 ± 5	796 ± 1

4. Discussion

4.1. Thin film crystal structure

The crystal structure of the films shifts from a mixed FCC and sigma phase to a single FCC phase with increased Mo content (Fig. 1). The sigma phase has been observed in CoCrFeNi films previously both at room temperature and with external heating, with and without Mo [26, 27, 34]. As the deposition was performed at room temperature, the adatoms from the plasma are not likely to diffuse once they have reached the substrate which could promote the formation of segregated secondary phases, i.e. the sigma phase. The formation of sigma phase seemed to be enhanced by small Mo additions (<2 at.%) as the sigma phase peak intensity in the x-ray diffractograms is higher for Mo2 compared to Mo0 (Fig. 1). When the Mo content is further increased, the sigma phase disappears, indicating the incorporation of Mo atoms (>2 at.%) in the FCC lattice inhibits the formation of sigma phase in addition to distorting the main FCC lattice. The opposite effect is observed for bulk alloys, e.g., increasing the Mo content promotes the sigma phase formation [35]. However, the phase formation in thin films differs from bulk alloys and higher amounts of Mo adatoms leads to incorporation of Mo in the main phase rather than formation of a separate phase.

As both the 304 L substrate and the films have an FCC structure there could be overlaps in the x-ray diffractogram (Fig. 1). However, EBSD analysis (Fig. 3b) confirmed that the films are (111) orientated. CoCrFeNi has been reported as highly (111) texturized when deposited at room temperature on Si (100) wafers [36, 37], indicating the films texture is independent of the substrate and is intrinsic to the material system itself. At higher deposition temperatures the mobility of the adatoms increases [38] and allows the grains of the films to grow in several orientations [21, 34].

4.2. Film growth and effect of Mo

The lattice of the films is distorted, a common effect observed for HEA and seen by the amounts of defects in the TEM images (Fig. 3c). The addition of Mo enhances the distortion and is evident here in the x-ray diffractograms by the shifts towards lower diffraction angles (Fig. 1). This distortion induces stress in the films. Because of the heterogeneous surface of the substrate due to cold rolling, the stress in the films could be unevenly distributed over the substrate grains and deformed areas.

The defects with an elongated structure in Mo0 seen in TEM images, grow onto the slip bands of the substrate (Fig. 3c and d). In SKPFM measurements the areas of the films grown on these slip bands have a different potential compared to the rest of the film, indicating the defects have indeed a different structure than the rest of the film, as seen for other HEA alloys with dual FCC/BCC structures [39]. The large Volta potential differences are only seen for Mo0 and Mo2, i.e. the films with the additional sigma phase. This could indicate that the defect rich areas over the slip bands are in fact the sigma phase. Such potential differences between the main phase and the sigma phase have been reported for duplex stainless steels [31]. Increasing the Mo content (> 2 at.%) suppresses the sigma phase formation and thus makes the film structure more homogenous.

4.3. Corrosion resistance

In the PD curves in Figs. 5 and 8 there is no active peak, i.e. current peak right after the corrosion potential. This shows that the passive film formed in contact with the electrolyte is stable enough to prevent dissolution of the metallic cations of the films into the electrolyte to reform a new passive layer. The native oxide acts as a chemical and physical barrier for the films [40]. The active peak in PD curves, i.e. native oxide dissolution, has been observed for CoCrFeNiMo alloys [35, 41], meaning the sputtered films in this study are highly stable in comparison. Mo inhibits the dissolution of Fe and Cr [41], two of the main elements of the films, which would explain the absence of the active peak. However, the active peak was not visible for the film without Mo which indicates the native oxide of the PVD films is very stable with and without Mo additions.

At 80 °C the difference in corrosion current density becomes more obvious compared to the room temperature measurements. Temperature is known to accelerate corrosion and the corrosion mechanisms can be better differentiated. The sigma phase seems to impact the corrosion resistance of the films, as significant improvement was observed at 80 °C for Mo > 2 at.%, i.e. when the sigma phase is absent. The phases with different crystal structure have different Volta potentials as seen in Fig. 4. This means the FCC phase is less noble than the sigma phase and preferential corrosion of the FCC phase would occur. Such behaviour have been observed for $\text{Al}_x\text{CoCrFeNi}$ alloys [39] and in our previous study of CoCrFe_xNi [34]. This suggests that preferential dissolution of less noble FCC phase over secondary sigma phase is the main mechanism in the early stages of corrosion at 80 °C for the Mo0–2 films. For Mo > 2 at.%, the films have only an FCC phase with a columnar structure, thus the passive film is more homogenous and stable, which results in a lower corrosion current density.

In the passive region, the passive film is mainly composed of Cr oxides and hydroxides (Fig. 7) which is typical for stainless steels [40, 42, 43] and CoCrFeNi alloys [20, 44]. For the Mo containing films, Mo (IV) and Mo(VI) oxides were also identified, which has also been observed for stainless steel 316 L and HEA alloys. The presence of these Mo oxides can stabilise the Cr oxide and hydroxide enriched passive film [35] and in our case improve the corrosion resistance as both corrosion and passive current densities decrease at 80 °C (Fig. 8 and Table 4). In austenitic stainless steels it is known that Mo reduces the dissolution rate of the passive film by forming Mo complexes with ions from the electrolyte thus enhances the passivation of the steels [15, 43]. It has also been shown that Mo homogenises the passive film of stainless steels by

forming nanostructures where local dissolutions have occurred [42]. The beneficial effect of Mo on the corrosion resistance has also been reported for CoCrFeNiMo alloys [18,35]. The enhanced corrosion properties of HEA alloys is also attributed to the decreased dissolution rates and thus decreased corrosion current densities for Mo containing alloy [19]. Furthermore, the incorporation of Mo oxides in the passive film provides stability to the Cr enriched passive film for CoCrFeNiMo alloys [20,41] and for coatings [23]. The effect of Mo was also observed in this study of CoCrFeNiMo sputtered films. The inhibition of Fe and Cr dissolution from the native oxide and the stabilisation by incorporation of Mo in the Cr enriched passive film are the two most likely reasons for this improvement of the corrosion resistance in the passive region.

The passive film undergoes a break-down in the transpassive region in Figs. 5 and 8, independent of Mo content. The sharp current increase at 0.85 V is assigned to the oxidation of Cr (III) to Cr (VI) species [32,45,46]. However, the passive film is able to repassivate as the current density decreases again at 1.3 V. This could be the formation of Fe₂O₃ based on the Pourbaix diagram of Fe [47] and that it can form in acidic solution [48]. Fe is present in the passive film in the passive region identified by XPS (Fig. 7) and could be oxidised once the Cr-oxide layer has been dissolved. After polarisation, the film without Mo has completely peeled off, whereas partially peeled off for Mo2–10 (Fig. 6). The inhibition of Fe and Cr dissolution by Mo is then more active and important in the transpassive region than in the passive region. The corrosion products on these films are believed to be HMoO₄⁻ and Fe₂O₃, the stable species for each metallic element in the Pourbaix diagrams. This once again shows the importance of Mo additions to the films as Mo could facilitate the repassivation and formation of the Fe enriched layer. The current density in the transpassive peak at 80 °C decreases more when the Mo content is increased. And as Mo reduces the dissolution rates of metallic cations, i.e. the current density, this could explain why the Mo containing films are better protected in the transpassive region and able to form stable corrosion products.

5. Conclusions

CoCrFeNiMo thin films were deposited on 304 L stainless steel substrates by DC magnetron sputtering. The effect of Mo additions on the structure of the films and their corrosion resistance in acidic environments was evaluated. The films with Mo content <2 at.% have a mixed FCC and sigma structure, whereas films with higher Mo content have a single FCC phase. All films have an FCC (111) texture. There are Volta potential differences for the Mo0 and Mo2 films in the different regions of the substrate. This was attributed to the different structures, i.e. FCC and sigma phase in the films. All films have a high corrosion resistance ($i_{\text{corr}} < 1 \mu\text{A}/\text{cm}^2$) at room temperature and at 80 °C. No significant differences in terms of corrosion and passive current densities were observed at room temperature. At 80 °C, the corrosion current density and passive current density decreased significantly for Mo content >2 at. %. This was attributed to the preferential dissolution of the FCC phase when the sigma phase is also present (Mo < 2 at%). XPS analysis of passivated films revealed that the passive film is mainly composed of Cr, Mo oxide and Cr hydroxide, which provided the high corrosion resistance.

CRedit authorship contribution statement

Clara Linder: Conceptualization, Investigation, Formal analysis, Writing – original draft, Writing – review & editing. **Smita G. Rao:** Conceptualization, Investigation, Formal analysis, Writing – review & editing. **Robert Boyd:** Investigation, Formal analysis, Writing – review & editing. **Grzegorz Greczynski:** Investigation, Formal analysis, Writing – review & editing. **Per Eklund:** Conceptualization, Supervision, Writing – review & editing, Funding acquisition. **Sara Munktel:** Conceptualization, Investigation, Formal analysis, Supervision, Writing – review & editing. **Arnaud le Febvrier:** Conceptualization, Writing –

review & editing. **Emma M. Björk:** Project administration, Conceptualization, Supervision, Writing – review & editing, Funding acquisition.

Declaration of competing interest

The authors declare that they have no known competing financial interests or personal relationships that could have appeared to influence the work reported in this paper.

Data availability

The data presented in this study are available on request to the corresponding author.

Acknowledgement

This study was performed within the Competence Centre FunMat-II and was funded by the Swedish Agency for Innovation Systems (VINNOVA, grant no 2016–05156, and grant no 2019–04881). The authors would also like to acknowledge the Swedish Government Strategic Research Area in Materials Science on Functional Materials at Linköping University (Faculty Grant SFO-Mat-LiU No. 2009 00971). The Centre in Nanoscience and Nanotechnology at LiTH (CeNano) at Linköping University is also acknowledged.

References

- [1] J.A. Okolie, B.R. Patra, A. Mukherjee, S. Nanda, A.K. Dalai, J.A. Kozinski, Futuristic applications of hydrogen in energy, biorefining, aerospace, pharmaceuticals and metallurgy, *Int. J. Hydrogen Energy*. 46 (2021) 8885–8905, <https://doi.org/10.1016/j.ijhydene.2021.01.014>.
- [2] R.A. Antunes, M.C.L. Oliveira, G. Ett, V. Ett, Corrosion of metal bipolar plates for PEM fuel cells: a review, *Int. J. Hydrogen Energy*. 35 (2010) 3632–3647, <https://doi.org/10.1016/j.ijhydene.2010.01.059>.
- [3] A. Coralli, B.J.M. Sarruf, P.E.V. De Miranda, L. Osmieri, S. Specchia, N.Q. Minh, Fuel Cells. Science and Engineering of Hydrogen-Based Energy Technologies: Hydrogen Production and Practical Applications in Energy Generation, Elsevier Inc, 2018, pp. 39–122, <https://doi.org/10.1016/B978-0-12-814251-6.00002-2>.
- [4] S. Porstmann, T. Wannemacher, W.G. Drossel, A comprehensive comparison of state-of-the-art manufacturing methods for fuel cell bipolar plates including anticipated future industry trends, *J. Manuf. Process*. 60 (2020) 366–383, <https://doi.org/10.1016/j.jmapro.2020.10.041>.
- [5] P. Malinowski, S. Fritze, L. Riekehr, L. von Fieandt, J. Cedervall, D. Rehnland, L. Nyholm, E. Lewin, U. Jansson, Synthesis and characterization of multicomponent (CrNbTaTiW)C films for increased hardness and corrosion resistance, *Mater. Des.* 149 (2018) 51–62, <https://doi.org/10.1016/j.matdes.2018.03.068>.
- [6] R. Shu, E.M. Paschalidou, S.G. Rao, J. Lu, G. Greczynski, E. Lewin, L. Nyholm, A. le Febvrier, P. Eklund, Microstructure and mechanical, electrical, and electrochemical properties of sputter-deposited multicomponent (TiNbZrTa)N_x coatings, *Surf. Coatings Technol.* 389 (2020) 1–7, <https://doi.org/10.1016/j.surfcoat.2020.125651>.
- [7] Y. Zou, H. Ma, R. Spolenak, Ultrastrong ductile and stable high-entropy alloys at small scales, *Nat. Commun.* (2015), <https://doi.org/10.1038/ncomms8748>.
- [8] B. Cantor, I.T.H. Chang, P. Knight, A.J.B. Vincent, Microstructural development in equiatomic multicomponent alloys, *Mater. Sci. Eng. A*. 375–377 (2004) 213–218, <https://doi.org/10.1016/j.msea.2003.10.257>.
- [9] J. Wang, W. Li, H. Yang, H. Huang, S. Ji, J. Ruan, Corrosion behavior of CoCrNi medium-entropy alloy compared with 304 stainless steel in H₂SO₄ and NaOH solutions, *Corros. Sci.* 177 (2020) 1–11, <https://doi.org/10.1016/j.corsci.2020.108973>.
- [10] I. Moravcik, N. Sadat, A. Motallebzadeh, Materials Characterization Interstitial nitrogen enhances corrosion resistance of an equiatomic CoCrNi medium-entropy alloy in sulfuric acid solution, *Mater. Charact.* 172 (2021) 1–10, <https://doi.org/10.1016/j.matchar.2020.110869>.
- [11] L. Wang, D. Mercier, S. Zanna, A. Seyeux, M. Laurent-Brocq, L. Perrière, I. Guillot, P. Marcus, Study of the surface oxides and corrosion behaviour of an equiatomic CoCrFeMnNi high entropy alloy by XPS and ToF-SIMS, *Corros. Sci.* 167 (2020) 108507, <https://doi.org/10.1016/j.corsci.2020.108507>.
- [12] X. wu Qiu, M. jun Wu, C. ge Liu, Y. peng Zhang, C. xiang Huang, Corrosion performance of Al₂CrFeCoCuNiTi high-entropy alloy coatings in acid liquids, *J. Alloys Compd.* 708 (2017) 353–357, <https://doi.org/10.1016/j.jallcom.2017.03.054>.
- [13] J. Wang, H. Yang, J. Ruan, Y. Wang, S. Ji, Microstructure and properties of CoCrNi medium-entropy alloy produced by gas atomization and spark plasma sintering, *J. Mater. Res.* 34 (2019) 2126–2136, <https://doi.org/10.1557/jmr.2019.96>.

- [14] Outokumpu, Handbook of Stainless Steel, 2013, pp. 1–89. <https://www.outokumpu.com/en/expertise/2021/handbook-of-stainless-steel>.
- [15] M. Kaneko, H.S. Isaacs, Effects of molybdenum on the pitting of ferritic- and austenitic-stainless steels in bromide and chloride solutions, *Corros. Sci.* 44 (2002) 1825–1834, [https://doi.org/10.1016/S0010-938X\(02\)00003-3](https://doi.org/10.1016/S0010-938X(02)00003-3).
- [16] P. Dhavveegan, N. Elangovan, T. Nishimura, N. Rajendran, Corrosion behavior of 316L and 304 stainless steels exposed to industrial-marine-urban environment: field study, *RSC Adv* 6 (2016) 47314–47324, <https://doi.org/10.1039/c6ra04015b>.
- [17] P. Lu, J.E. Saal, G.B. Olson, T. Li, O.J. Swanson, G.S. Frankel, A.Y. Gerard, K. F. Quiambao, J.R. Scully, Computational materials design of a corrosion resistant high entropy alloy for harsh environments, *Scr. Mater.* 153 (2018) 19–22, <https://doi.org/10.1016/j.scriptamat.2018.04.040>.
- [18] Q. Wang, A. Amar, C. Jiang, H. Luan, S. Zhao, H. Zhang, G. Le, X. Liu, X. Wang, X. Yang, J. Li, CoCrFeNiMo_{0.2} high entropy alloy by laser melting deposition: prospective material for low temperature and corrosion resistant applications, *Intermetallics* 119 (2020) 1–6, <https://doi.org/10.1016/j.intermet.2020.106727>.
- [19] W. Wang, J. Wang, H. Yi, W. Qi, Q. Peng, Effect of molybdenum additives on corrosion behavior of high-entropy alloys CoCrFeNiMo_x in aqueous environments, *Entropy* 20 (2018) 908, <https://doi.org/10.3390/e20120908>.
- [20] X.L. Shang, Z.J. Wang, Q.F. Wu, J.C. Wang, J.J. Li, J.K. Yu, Effect of Mo addition on corrosion behavior of high-entropy alloys CoCrFeNiMo_x in aqueous environments, *Acta Metall. Sin. (English Lett.)* 32 (2019) 41–51, <https://doi.org/10.1007/s40195-018-0812-7>.
- [21] C. Dai, Y. Fu, J. Guo, C. Du, Effects of substrate temperature and deposition time on the morphology and corrosion resistance of FeCoCrNiMo_{0.3} high-entropy alloy coating fabricated by magnetron sputtering, *Int. J. Miner. Metall. Mater.* 27 (2020) 1388–1397, <https://doi.org/10.1007/s12613-020-2149-2>.
- [22] F. Fanicchia, I. Csaki, L.E. Geambazu, H. Begg, S. Paul, Effect of microstructural modifications on the corrosion resistance of CoCrFeMo_{0.85}Ni compositionally complex alloy coatings, *Coatings* 9 (2019) 695.
- [23] H. Wu, S. Zhang, Z.Y. Wang, C.H. Zhang, H.T. Chen, J. Chen, New studies on wear and corrosion behavior of laser cladding FeNiCoCrMox high entropy alloy coating: the role of Mo, *Int. J. Refract. Met. Hard Mater.* 102 (2022) 105721, <https://doi.org/10.1016/j.jrmm.2021.105721>.
- [24] A. le Febvrier, L. Landalv, T. Liersch, D. Sandmark, P. Sandstrom, P. Eklund, An upgraded ultra-high vacuum magnetron-sputtering system for high-versatility and software-controlled deposition, *Vacuum* 187 (2021) 110137, <https://doi.org/10.1016/j.vacuum.2021.110137>.
- [25] G. Greczynski, L. Hultman, Compromising science by ignorant instrument calibration—need to revisit half a century of published XPS data, *Angew. Chemie - Int. Ed.* 59 (2020) 5002–5006, <https://doi.org/10.1002/anie.201916000>.
- [26] Y. Qiu, M.A. Gibson, H.L. Fraser, N. Birbilis, Corrosion characteristics of high entropy alloys, *Mater. Sci. Technol.* 31 (2015) 1235–1243, <https://doi.org/10.1179/1743284715Y.0000000026>.
- [27] M.K. Kini, S. Lee, A. Savan, B. Breitbach, Y. Addab, W. Lu, M. Ghidelli, A. Ludwig, N. Bozzolo, C. Scheu, D. Chatain, G. Dehm, Nanocrystalline equiatomic CoCrFeNi alloy thin films: are they single phase fcc? *Surf. Coatings Technol.* 410 (2021) 126945 <https://doi.org/10.1016/j.surfcoat.2021.126945>.
- [28] F. Popa, I. Chicinaş, D. Frunză, I. Nicodim, D. Banabic, Influence of high deformation on the microstructure of low-carbon steel, *Int. J. Miner. Metall. Mater.* 21 (2014) 273–278, <https://doi.org/10.1007/s12613-014-0905-x>.
- [29] K.A. Nibur, D.F. Bahr, Identifying slip systems around indentations in FCC metals, *Scr. Mater.* 49 (2003) 1055–1060, <https://doi.org/10.1016/j.scriptamat.2003.08.021>.
- [30] S.G. Rao, B. Mukhamedov, G. Nagy, E.N. Tseng, R. Shu, R. Boyd, D. Primetzhofer, P.O.Å. Persson, B. Alling, I.A. Abrikosov, A. Febvrier, P. Eklund, Phase formation in CrFeCoNi nitride thin films, *Phys. Rev. Mater.* 7 (2023) 1–11, <https://doi.org/10.1103/PhysRevMaterials.7.055002>.
- [31] N. Sathirachinda, R. Pettersson, J. Pan, Depletion effects at phase boundaries in 2205 duplex stainless steel characterized with SKPFM and TEM/EDS, *Corros. Sci.* 51 (2009) 1850–1860, <https://doi.org/10.1016/j.corsci.2009.05.012>.
- [32] E.-M. Paschalidou, R. Lindblad, L.Z. Medina, D. Karlsson, U. Jansson, L. Nyholm, Corrosion studies on multicomponent CoCrFeMnNi(C) thin films in acidic environments, *Electrochim. Acta* 404 (2021) 139756, <https://doi.org/10.1016/j.electacta.2021.139756>.
- [33] K.D. Bomben, J.F. Moulder, W.F. Stickle, P.E. Sobol, X-ray Photoelectron Spectroscopy (XPS), 1992, <https://doi.org/10.1002/0470014229.ch22>.
- [34] C. Linder, S.G. Rao, R.D. Boyd, A. Le Febvrier, P. Eklund, S. Munktel, E.M. Björk, Corrosion resistance and catalytic activity toward the oxygen reduction reaction of CoCrFeNi (0 ≤ x ≤ 0.7) thin films, *ACS Appl. Energy Mater.* 5 (2022) 10838–10848, <https://doi.org/10.1021/acsaem.2c01499>.
- [35] X. Wang, D. Mercier, Y. Danard, T. Rieger, L. Perrière, M. Laurent-Brocq, I. Guillot, V. Maurice, P. Marcus, Enhanced passivity of Cr-Fe-Co-Ni-Mo multi-component single-phase face-centred cubic alloys: design, production and corrosion behaviour, *Corros. Sci.* 200 (2022), <https://doi.org/10.1016/j.corsci.2022.110233>.
- [36] J.J. Wang, F.Y. Ouyang, Nanotwinned medium entropy alloy CoCrFeNi thin films with ultra-high hardness: modifying residual stress without scarifying hardness through tuning substrate bias, *Surf. Coatings Technol.* 434 (2022) 128191, <https://doi.org/10.1016/j.surfcoat.2022.128191>.
- [37] N. Chawake, J. Zálesák, C. Gammer, R. Franz, M.J. Cordill, J.T. Kim, J. Eckert, Microstructural characterization of medium entropy alloy thin films, *Scr. Mater.* 177 (2020) 22–26, <https://doi.org/10.1016/j.scriptamat.2019.10.001>.
- [38] J.E. Greene, Chapter 12 - Thin Film Nucleation, Growth, and Microstructural Evolution: An Atomic Scale View, 3rd Edit, William Andrew Publishing, 2010, <https://doi.org/10.1016/B978-0-8155-2031-3.00012-0>.
- [39] Y. Shi, L. Collins, R. Feng, C. Zhang, N. Balke, P.K. Liaw, B. Yang, Homogenization of AlxCoCrFeNi high-entropy alloys with improved corrosion resistance, *Corros. Sci.* 133 (2018) 120–131, <https://doi.org/10.1016/j.corsci.2018.01.030>.
- [40] E. Mattsson, V. Kučera, Elektrokemi Och Korrosionslära, Swerea KIMAB, Swedish, 2009.
- [41] C. Dai, H. Luo, J. Li, C. Du, Z. Liu, J. Yao, X-ray photoelectron spectroscopy and electrochemical investigation of the passive behavior of high-entropy FeCoCrNiMox alloys in sulfuric acid, *Appl. Surf. Sci.* 499 (2020) 143903, <https://doi.org/10.1016/j.apsusc.2019.143903>.
- [42] V. Maurice, H. Peng, L.H. Klein, A. Seyeux, S. Zanna, P. Marcus, Effects of molybdenum on the composition and nanoscale morphology of passivated austenitic stainless steel surfaces, *Faraday Discuss* 180 (2015) 151–170, <https://doi.org/10.1039/c4fd00231h>.
- [43] L. Wegrelus, F. Falkenberg, I. Olefjord, Passivation of Stainless Steels in Hydrochloric Acid, *J. Electrochem. Soc.* 146 (1999) 1397–1406.
- [44] Y. Lou, C. Dai, W. Chang, H. Qian, L. Huang, C. Du, D. Zhang, Microbiologically influenced corrosion of FeCoCrNiMo_{0.1} high-entropy alloys by marine *Pseudomonas aeruginosa*, *Corros. Sci.* 165 (2020), <https://doi.org/10.1016/j.corsci.2019.108390>.
- [45] T. Li, O.J. Swanson, G.S. Frankel, A.Y. Gerard, P. Lu, J.E. Saal, J.R. Scully, Localized corrosion behavior of a single-phase non-equimolar high entropy alloy, *Electrochim. Acta* 306 (2019) 71–84, <https://doi.org/10.1016/j.electacta.2019.03.104>.
- [46] S. Neupane, S. Zanna, A. Seyeux, L.H. Klein, V. Maurice, P. Marcus, Can We Enhance Passivity with a Surface Finish? Spectroscopic and Electrochemical Analysis on 316L Stainless Steel, *J. Electrochem. Soc.* 169 (2022) 011505, <https://doi.org/10.1149/1945-7111/ac4bf7>.
- [47] M. Pourbaix, Atlas of Electrochemical Equilibria in Aqueous Solutions, 1974, <https://doi.org/10.4028/www.scientific.net/msf.251-254.143>.
- [48] J.R. Scully, K. Lutton, Polarization Behavior of Active Passive Metals and Alloys, *Encycl. Interfacial Chem. Surf. Sci. Electrochem.* (2018) 439–447, <https://doi.org/10.1016/B978-0-12-409547-2.13393-1>.